

# Discrimination between prompt and long-lived particles using convolutional neural network

---

**Biplob Bhattacharjee<sup>a</sup> Swagata Mukherjee<sup>b</sup> Rhitaja Sengupta<sup>a</sup>**

<sup>a</sup>*Centre for High Energy Physics, Indian Institute of Science,  
Bangalore 560012, India*

<sup>b</sup>*III. Physikalisches Institut A, RWTH Aachen University,  
Otto-Blumenthal-Str. 16, 52074 Aachen, Germany*

*E-mail:* [biplob@iisc.ac.in](mailto:biplob@iisc.ac.in), [mukherjee@physik.rwth-aachen.de](mailto:mukherjee@physik.rwth-aachen.de),  
[rhitaja@iisc.ac.in](mailto:rhitaja@iisc.ac.in)

**ABSTRACT:** Sophisticated machine learning techniques, like computer vision, are state of the art in modern day research. These technologically advanced algorithms have promising potential in search for physics beyond Standard Model in Large Hadron Collider (LHC). Most of the computer vision tasks are surrounded around convolutional neural networks (CNN), which can provide powerful tools for differentiating between patterns of calorimeter energy deposits by prompt particles of Standard Model and long-lived particles predicted in various models beyond the Standard Model. We demonstrate the usefulness of CNN by using a couple of physics examples from well motivated BSM scenarios predicting long-lived particles giving rise to displaced jets. Our work suggests that modern machine-learning techniques have potential to discriminate between energy deposition patterns of prompt and long-lived particles, and thus, they can be useful tools in such searches.

**KEYWORDS:** Machine learning, CNN, Computer vision, Long-lived particle, BSM

---

## Contents

<b>1</b>	<b>Introduction</b>	<b>1</b>
<b>2</b>	<b>Understanding the displaced features of LLPs using images</b>	<b>3</b>
2.1	Segmentation of the calorimeter	4
2.2	Two displaced scenarios and their energy deposition patterns	5
2.2.1	Displaced jets from displaced SM $Z$ boson	7
2.2.2	Displaced jets directly from LLP decay	11
2.3	The Convolution Neural Network	14
2.3.1	Network Architecture	14
2.3.2	Dataset	15
2.4	Analysis and Results	15
2.4.1	Displaced jets from displaced $Z$	15
2.4.2	Displaced jets directly from LLP decay	17
<b>3</b>	<b>Conclusion and Outlook</b>	<b>20</b>

---

## 1 Introduction

The Standard model (SM) of particle physics is an extremely successful model in describing the interactions between known elementary particles. However, it cannot be a complete theory, because it does not address several open questions as well as observations in particle physics, such as neutrino oscillations, matter-antimatter asymmetry, dark matter, etc. This implies that new particles beyond the Standard Model (BSM) should exist. Current BSM search programs in LHC experiments mostly focus on energetic final states produced at the interaction point (IP). However, the existing searches are largely insensitive to Long-Lived Particles (LLPs), which decay into SM particles some macroscopic distance away from the IP. Particles with macroscopic lifetimes are ubiquitous in the SM, and the same mechanisms could be present in any BSM theory. Theories with LLPs, such as many versions of hidden sectors or hidden valleys [1–5], SUSY [6–15], WIMP Baryogenesis [16, 17], neutrino extensions [18–21] etc., can address some or all of the fundamental shortcomings of the SM. Despite the strong motivations, LLPs mostly remain unexplored by standard LHC searches, although in recent years these particles have attracted growing interest, and some dedicated searches have been performed in LHC experiments [22–34].<sup>1</sup>

LHC searches depend on reconstruction of objects, like photons, electrons, muons and jets, in an event. These reconstructions are based on standard algorithms taking information from different parts of the detectors. In collider experiments, the calorimeters

---

<sup>1</sup>A comprehensive overview of LLP signatures at LHC and recent searches can be found in [34] and the references therein.

(both electromagnetic, ECAL and hadronic, HCAL) are segmented in  $\eta - \phi$  towers in such a way that a single particle coming from the primary vertex usually falls within a single calorimeter tower corresponding to the particle's actual  $\eta$  and  $\phi$ . For LLPs, where the particles have long lifetimes and therefore decay after travelling sufficiently longer distances, the situation may differ. If the decay products are displaced enough, then their  $\eta$  and  $\phi$  directions (which start from the secondary vertex) may not match with the standard  $\eta - \phi$  segmentation of the detectors. Therefore a particle is no longer guaranteed to be concentrated to a single  $\eta - \phi$  tower. Rather, it may be spread over several  $\eta - \phi$  towers (as shown in Fig. 1). This feature was studied for displaced photons which look quite different in the ECAL than the prompt ones [35]. One might then expect that this effect will be more prominent for displaced jets which contain many particles; and the energy deposition in the HCAL should be different from standard patterns observed for prompt jets. However, it may be the case that many particles actually smear out this effect, or, that we don't see such effects due to the coarser resolution of the HCAL, compared to ECAL. Therefore we attempt to study how displaced jets look in the HCAL and understand their different features.

Long lived particles which are color-neutral will decay to two or more quarks or gluons, and therefore, we will have more than one displaced jet in the final state. If the LLP has color charge, it will most probably hadronise before decaying (when the QCD phase-transition scale is greater than the decay width of the LLP, i.e.,  $\Lambda_{QCD} > \Gamma$ ). These hadrons are again color neutral objects which later decay to give multiple jets. Therefore, we mostly land up with at least two displaced jets in the final state. Standard displaced jets analysis of ATLAS and CMS loses its sensitivity as the distance between the IP and the secondary vertex increases. This is because these displaced jets will most probably have different energy deposition patterns in the HCAL compared to the standard pattern we usually see for prompt jets as discussed above. This makes the reconstruction of these displaced jets challenging as the decay length of the LLP increases. Even with a few tweaks in the reconstruction algorithm, this task is quite arduous. It may be the case that in present experiments, we mostly lose such LLP events with standard reconstruction techniques, and thus end up with low signal efficiency. Typical signal efficiency in analyses involving displaced jets signature in LHC experiments is often in the ballpark of a few percent [22].

In this work, we take a step back from reconstructing jets to just studying their energy deposition patterns in the HCAL. For that we have simulated a toy calorimeter closely resembling the barrel HCAL of the ATLAS detector. We consider two scenarios. First, displaced SM  $Z$  boson coming from the decay of an LLP and further decay of  $Z$  to give displaced jets and second, displaced jets directly coming from the decay of an LLP. These two scenarios have some kinematic differences due to the presence of an on-shell intermediate state ( $Z$  boson) in the former unlike the latter. We also make both the scenarios boosted enough to bring all the LLP decay products closer such that they can be viewed together in the calorimeter. We consider distributions of energy fraction deposited in  $\eta - \phi$  regions of various sizes and find these distributions to have some differences for different displacements of the LLP. This motivates us to look for modern ways of classifying LLP and non-LLP scenarios using the difference in energy deposition pattern.

Machine learning has recently shown great results in many disciplines and has a variety of applications. It offers the potential to automate challenging data-processing tasks, and classification in high-dimensional variable spaces in collider physics [36]. Neutrino experiments like NOvA [37] and MicroBooNE [38] used computer-vision techniques to reconstruct and classify various types of neutrino events. Our approach builds upon the paradigm that a substantial energy deposit in HCAL, coming from a SM particle or from a BSM particle, can be treated as an image, with intensity given by the amount of energy deposit in HCAL. One straight-forward approach to process the LHC data is the jet images approach discussed in references [39, 40]. The idea behind jet images is to treat the energy deposits in a calorimeter as intensities in a 2D image. Then one can apply sophisticated algorithms developed for image recognition. This and related neural network approaches were used for boosted  $W$  boson tagging [41], top tagging [42–45], generic anti-QCD tagging [46, 47], photon identification [48], heavy-flavor tagging [49] and search for BSM particles [50–55]. Modern deep learning algorithms trained on HCAL energy deposition images can be used for LLP studies. We use convolutional neural network (CNN), a supervised learning algorithm which is specifically designed for working with images. We train a CNN to identify the features associated with displaced jets so that it can distinguish the LLP events from non-LLP ones based on the images of energy deposition patterns in the HCAL.

To the best of our knowledge, this work is the first attempt in studying LLPs using image recognition algorithms like convolutional neural networks. We have used minimal preprocessing to the images and have not done advanced optimisations in this work since our goal is just to understand the differences in energy deposition due to displacement and further optimisations might achieve better discrimination. This paper is outlined as follows: in section 2.1, we present the segmentation of the HCAL used by us; in section 2.2, we discuss the two displaced scenarios: displaced  $Z$  boson and displaced jets coming directly from the decay of an LLP. We also discuss the change in pattern of energy deposition with displacement using distributions of energy fractions for the two scenarios and identify the key features associated with displaced multijet systems; in section 2.3, we describe the CNN architecture used by us and other details related to the network training, validation and testing; the analysis and results are presented in section 2.4 where we check the effect of mass of the LLP in the displaced  $Z$  scenario and also present a brief discussion on stopped particle scenario as a special case of the second displaced scenario described above, in which the LLP stops in the HCAL and then decays to give jets; finally in section 3, we conclude.

## 2 Understanding the displaced features of LLPs using images

The main motive of this work is to study whether displaced jets coming from color neutral LLPs have any difference in energy deposition patterns in the HCAL from standard prompt jets. Furthermore, if there is any difference, we need to know whether this difference is significant enough so that ordinary analyses with cuts can distinguish between them or does it call for the need to employ image recognition techniques for such discrimination. These differences may also depend on various LLP models and mass of the LLP. In this work we aim to address such questions. We will identify the features associated with only

the displacement of jets and therefore, compare the non-displaced and displaced cases of the same model. We will do the same for both the scenarios which are described in section 1 to find out how the difference in these two scenarios highlight slightly different features of displaced multijet systems.

For observing features associated with displacement of a particle, we have to consider the actual segmentation of the calorimeter. The usual analysis with fast detector simulation (for example, **Delphes**) which only has  $\eta - \phi$  segmentation of the calorimeters won't work here because it has no layered calorimeter structure and no segmentation in the physical  $z$  direction. Such detector simulations give the actual  $\eta - \phi$  of the LLP decay products. As a result, we don't get the effects of displaced particles as discussed in section 1 which arises due to projection of radial layers taken along constant  $\eta - \phi$  directions and also due to segmentation in  $z$  direction. Therefore, for the illustration of our idea, we simulate a simplified calorimeter with segmentation close to that of the ATLAS HCAL. We start by discussing the segmentation of our toy calorimeter in the next section.

## 2.1 Segmentation of the calorimeter

In this section, we explain the segmentation of the HCAL that we have considered here and also elucidate how we propagate the particles and parametrise their energy deposition in each tower of the calorimeter.

For the segmentation part, we closely follow the Tile Calorimeter [56] of the ATLAS detector which has four layers, viz., A, B, C and D, arranged along the radial direction, one after the other, with segmentations in the  $\eta - \phi$  directions. The  $\phi$  direction is segmented into 64 parts – each segment being close to 0.1 radian. For segmentation in the  $\eta$  direction, we take the segment size to be 0.1 radian for layers A, B and C, and 0.2 radian for layer D, the same as ATLAS. Now to translate this  $\eta$  segmentation into  $z$  segmentation, we segment along the  $z$  points where the constant  $\eta$  lines (0.1 radian apart) cut the radial central line of each layer – same as done in the Tile Calorimeter. We have shown in Fig. 1 the segmentation of the calorimeter along the  $z$  direction with constant  $\eta$  lines for reference. In the  $z$ -direction, we extend upto  $|z| = 6$  m which corresponds to the barrel region of the ATLAS HCAL detector. This gives a pseudorapidity coverage of about  $|\eta| < 1.7$ .<sup>2</sup>

We now generate events of physical processes and use the **ParticlePropagator** code in **Delphes-3.4.1** [57] to propagate the particles to the starting of layer A of the HCAL. If the particle is having  $|z| > 6$  m already by then, we ignore it. We also ignore electrons, muons and neutrinos. We then propagate each particle further to find out the  $\eta - \phi$  bins of the HCAL traversed by the particle and store the energy deposited by the particle in each of these bins. The energy deposited in each bin is inversely proportional to the distance travelled by the particle in that bin. This is done for all the particles in an event and then projection is taken along constant  $\eta$  and  $\phi$  directions of all the four layers. This gives us energy deposition in the  $\eta - \phi$  plane which is divided into  $32 \times 64$  towers.

---

<sup>2</sup>The pseudorapidity coverage of the calorimeter can be extended by following the segmentation of the end-cap parts of the Tile Calorimeter. In this work, we restrict to the barrel region of the calorimeter.

## Segmentation of the HCAL

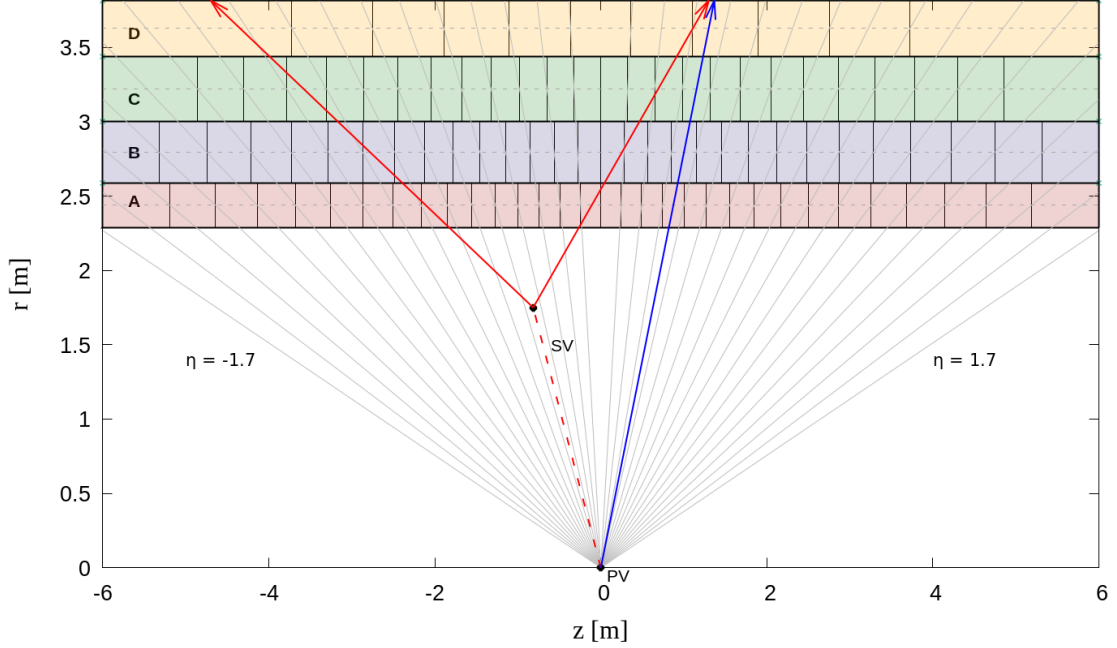


**Figure 1:** Simplified segmentation of the HCAL used in this work – A,B,C and D are the four radial layers extending from 2.2895 m to 3.8158 m and has a pseudorapidity coverage of  $|\eta| < 1.7$ . Constant  $\eta$  lines are shown in gray for reference. A standard particle coming from the Primary Vertex (PV) is shown in blue. A long-lived particle coming from PV and its decay products starting from the secondary vertex (SV) are shown in red. Note that the particle in blue is contained within a single  $\eta$  tower (between two grey lines) whereas the particles in red are spread over several  $\eta$  towers.

Any tower of the HCAL having energy deposit less than 1 GeV is ignored. We normalise the energy in each tower of an event using the maximum<sup>3</sup> energy deposited in the HCAL for that event. We store the energy deposition of an event as a 28 pixel $\times$ 28 pixel image with the energy depositions in each tower as intensity values of each pixel of the image with the highest intensity (energy) pixel at the centre of the  $i\eta - i\phi$ <sup>4</sup> plane. We use these images as our input to the neural network.

## 2.2 Two displaced scenarios and their energy deposition patterns

In this section, we describe the two displaced scenarios considered by us for this work and their simulation details. We also discuss the difference in their energy deposition patterns in the HCAL and how and why this pattern changes with displacement.

<sup>3</sup>We have also normalised the images with the energy sum of each event and repeated the analysis. This has negligible effect on our results.

<sup>4</sup> $i\eta$  and  $i\phi$  implies the bin number in the  $\eta - \phi$  directions respectively. We use this notation to denote pixels of the images.

Using the segmentation process described in section 2.1, we now have  $28 \times 28$  images of energy deposition in the calorimeter for the following four cases:

- particles from the PV, hence, not displaced;
- particles from a transverse distance between 30 cm and 50 cm;
- particles from a transverse distance between 50 cm and 70 cm;
- particles from a transverse distance between 70 cm and 90 cm;
- particles from a transverse distance between 200 cm and 220 cm,

where the first four are cases of LLP decay within the Tracker and the last one corresponds to decay of the LLP just before entering the HCAL. Hereafter, whenever we mention displacement of particles, we mean displacement in the transverse direction, unless otherwise stated.

To study the difference in energy deposition pattern with displacement, we consider the following distributions:

$$f_i, \quad i = 3, 5, 9, 11$$

where  $f_i$  is the fraction of energy deposited in  $i \times i$  block of the full  $28 \times 28$  image. This  $i \times i$  block's centre is anchored to the centre of the  $28 \times 28$  image.

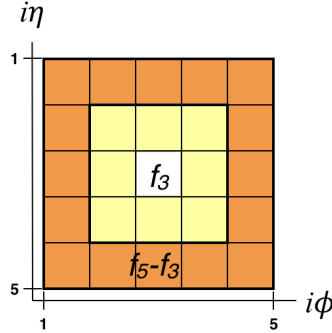


**Figure 2:** Central  $5 \times 5$  part of the  $28 \times 28$   $i\eta - i\phi$  image. The fraction of total energy (in  $28 \times 28$   $i\eta - i\phi$  region) deposited in this part is  $f_5$ . The central  $3 \times 3$  part has energy fraction  $f_3$  (yellow and white) and the rest has energy fraction  $f_5 - f_3$  (orange).  $f_3$  contains the central highest energy tower (shown in white).

Fig. 2 illustrates the meaning of  $f_3$  and  $f_5 - f_3$ . We will consider distributions of the energy fraction  $f_3$  which includes the central highest energy tower; and exclusive energy fractions – energy deposition fraction in  $i \times i$  block excluding the previous block's energy fraction (like  $f_5 - f_3$ ,  $f_9 - f_5$ ,  $f_{11} - f_9$  and so on <sup>5</sup>) to study differences in energy deposition patterns with displacement.

<sup>5</sup>We have also studied distributions of exclusive energy fractions involving  $f_{15}$ ,  $f_{21}$  and  $f_{28}$ . These exclusive regions have very little energy deposits for most events and follow the same trend as  $f_{11} - f_9$ .



### 2.2.1 Displaced jets from displaced SM $Z$ boson

The first scenario considered in this work is displaced jets from the decay of a boosted  $Z$  boson, which again comes from the decay of a long-lived particle  $X$ . Hence, the  $Z$  boson is displaced. From here on, we will refer to the LLP as  $X$  throughout the subsequent sections. We consider that the  $X$  decays to SM  $Z$  boson and any invisible particle  $Y$ .

$$X \text{ (LLP)} \rightarrow Z \text{ (SM)} + Y \text{ (Invisible)}$$

To simulate such a process, we use the gauge mediated SUSY breaking model [6, 58], where the neutralino is long-lived and decays to SM  $Z$  boson and light gravitino which is invisible to the detector. We consider the case where the  $Z$  boson decays to quarks,  $Z \rightarrow qq$  and are interested to check the pictorial view of energy deposition of this  $Z \rightarrow qq$ , where the  $Z$  is displaced since it's coming from the LLP decay, in HCAL in  $\eta - \phi$  plane.

We use PYTHIA6 [59] for generation of events. We consider a non-displaced  $Z$  scenario in which the particle  $X$  is not long-lived and therefore decays at the PV and displaced  $Z$  scenario (coming from long-lived  $X$ ) which again we divide in four categories as described in the starting of section 2.2. Also, to ensure that the decay products fall mostly within the calorimeter segment, we put a condition that the longitudinal displacement is less than 200 cm. For comparing the different displaced and non-displaced cases, we apply an energy window cut and restrict to events where the total HCAL deposit inside the  $28 \times 28$  part of the  $i\eta - i\phi$  plane is between (400, 500) GeV for the non-displaced as well as all the displaced cases. The choice of this particular energy range is made to have boosted  $Z$  bosons. Boost is required to bring the displaced jets closer in the  $\eta - \phi$  plane.

Fig. 3 shows the normalised distributions of energy fractions for the non-displaced and the different displaced cases discussed above. Fig. 3a shows the energy fraction deposited in  $3 \times 3$  block of the full image,  $f_3$ . To understand the feature shown by these distributions, let's first observe the non-displaced case and the first three displaced cases where  $X$  decays within Tracker. There are only small differences in the distributions of  $f_3$  with displacement for these cases. As we move to the energy deposited after this  $3 \times 3$  block but within a  $5 \times 5$  block,  $f_5 - f_3$ , we note in Fig. 3b that the non-displaced  $Z$  has relatively smaller energy deposition fraction in this region than the displaced  $Z$  cases. In the next  $9 \times 9$  block (exclusive of the  $5 \times 5$ ),  $f_9 - f_5$ , we see from Fig. 3c that the non-displaced  $Z$  distribution has caught up with the displaced cases and again the difference is small. But for the next  $11 \times 11$  block,  $f_{11} - f_9$ , we find that the non-displaced  $Z$  has higher energy fractions than the displaced cases (Fig. 3d).

The change in these distributions corresponds to the fact that there are two distinct objects present in the decay of the  $Z$  boson and there is a finite gap between these two jets in the  $\eta - \phi$  plane. The distribution of  $f_5 - f_3$  is falling faster than the  $f_9 - f_5$  distribution and the latter has a small hump around 30–40% energy fraction, implying that the second decay product mostly lies within the region between  $5 \times 5$  and  $9 \times 9$  in the  $i\eta - i\phi$  plane. For the displaced  $Z$  boson these objects are spread over the  $\eta - \phi$  plane and there is a chance of overlap. Greater the displacement, greater is the chance of such an overlap and therefore the gap is not prominent for displaced cases. This explains the fact that the



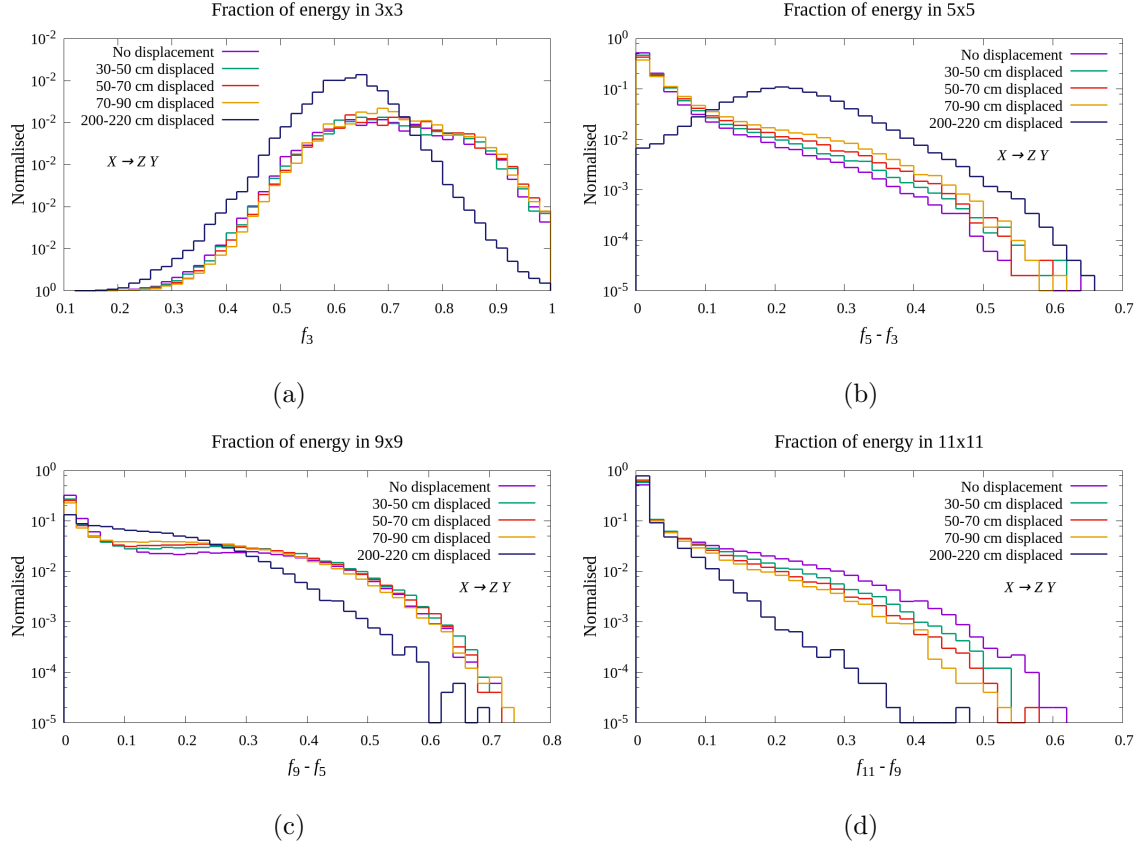


**Figure 3:** Normalised distributions of energy deposition fraction ( $f_i$ ) with varying sizes of blocks ( $i \times i$ ). (a) Fraction of energy deposited in  $3 \times 3$ ; (b),(c),(d) Fraction of energy deposited in  $5 \times 5$ ,  $9 \times 9$  and  $11 \times 11$  excluding the previous  $3 \times 3$ ,  $5 \times 5$  and  $9 \times 9$  blocks' energy deposition fraction respectively.

$f_5 - f_3$  distribution falls off faster for the prompt  $Z$  than the  $70 - 90$  cm displaced  $Z$ . Also, the  $f_{11} - f_9$  distribution falls much faster for the displaced cases, implying that their total energy deposit is mostly contained within smaller  $i\eta - i\phi$  region. The energy deposit of the second object shifts to more smaller  $i\eta - i\phi$  blocks with increasing displacement. Looking at the distributions for the  $200 - 220$  cm displaced  $Z$ , we find that the containment of the total energy deposit within smaller  $i\eta - i\phi$  regions is more prominent here and the second object mostly lies between the  $3 \times 3$  and  $5 \times 5$  blocks as is evident from the peak in  $f_5 - f_3$  distribution.

Fig. 4 shows the average of 50,000  $Z$  boson images for each of the cases where the decay is within the Tracker. For the non-displaced  $Z$  (Fig. 4a), there is a clear annulus of the  $Z$  boson coming from the second decay product. We observe that statistically these energy deposits look different. The distance between the two energy deposits corresponding to the two jets keeps decreasing with displacement and the overall size of the total energy deposit also becomes slightly smaller with increasing displacement. We have explained these displacement features at the end of section 2.2.2 after discussing the energy deposition

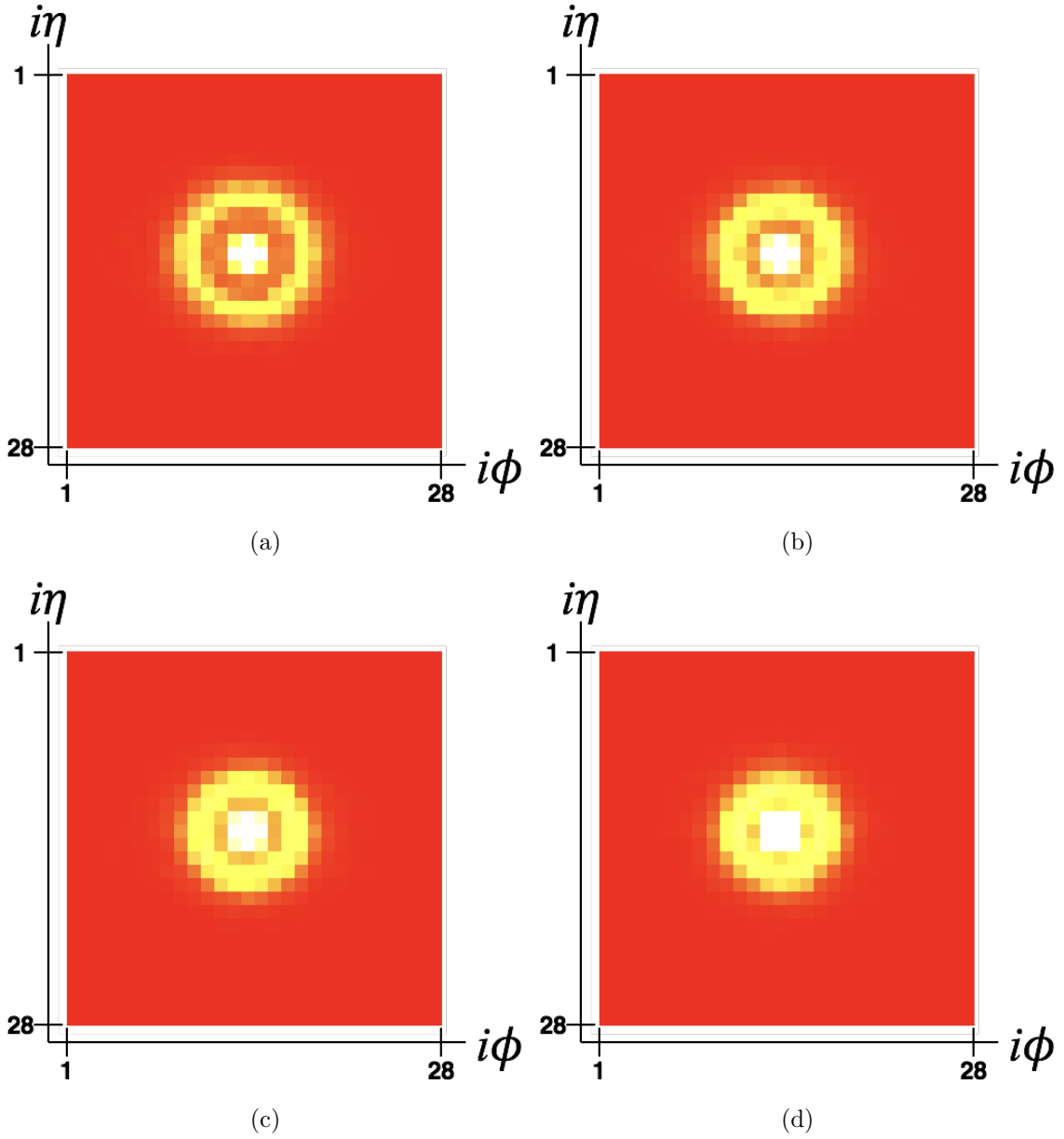


**Figure 4:** Average of 50,000 images for (a)  $Z$  boson with no displacement; (b), (c), (d)  $Z$  boson displaced within transverse distance of 30 – 50 cm, 50 – 70 cm and 70 – 90 cm from PV respectively. These are  $28 \times 28$  images in the  $i\eta - i\phi$  plane with the highest energy bin in the center (14,14). With increasing displacement, the distance between two jets decreases, as seen from the figures.

pattern of the second scenario.

Although statistically the difference between the displaced and prompt case is noticeable as is observed by the average images (Fig. 4), we need to check whether this difference is that prominent for individual images. Fig. 5 shows nine typical images for jets coming

from a prompt  $Z$  (Fig. 5a), and jets coming from 50 – 70 cm displaced  $Z$  (Fig. 5b) and from 200 – 220 cm displaced  $Z$  (Fig. 5c). We find that with increasing displacement, the energy deposits become more elongated and overall the multijet system is more contained. These features can easily be seen for the 200 – 220 cm displaced  $Z$ , but are not that prominent for the 50 – 70 cm displaced  $Z$ . Also, even the prompt case has some events where the energy depositions have some elongations. Therefore, it is not always possible to discriminate between them when we are given these individual images.

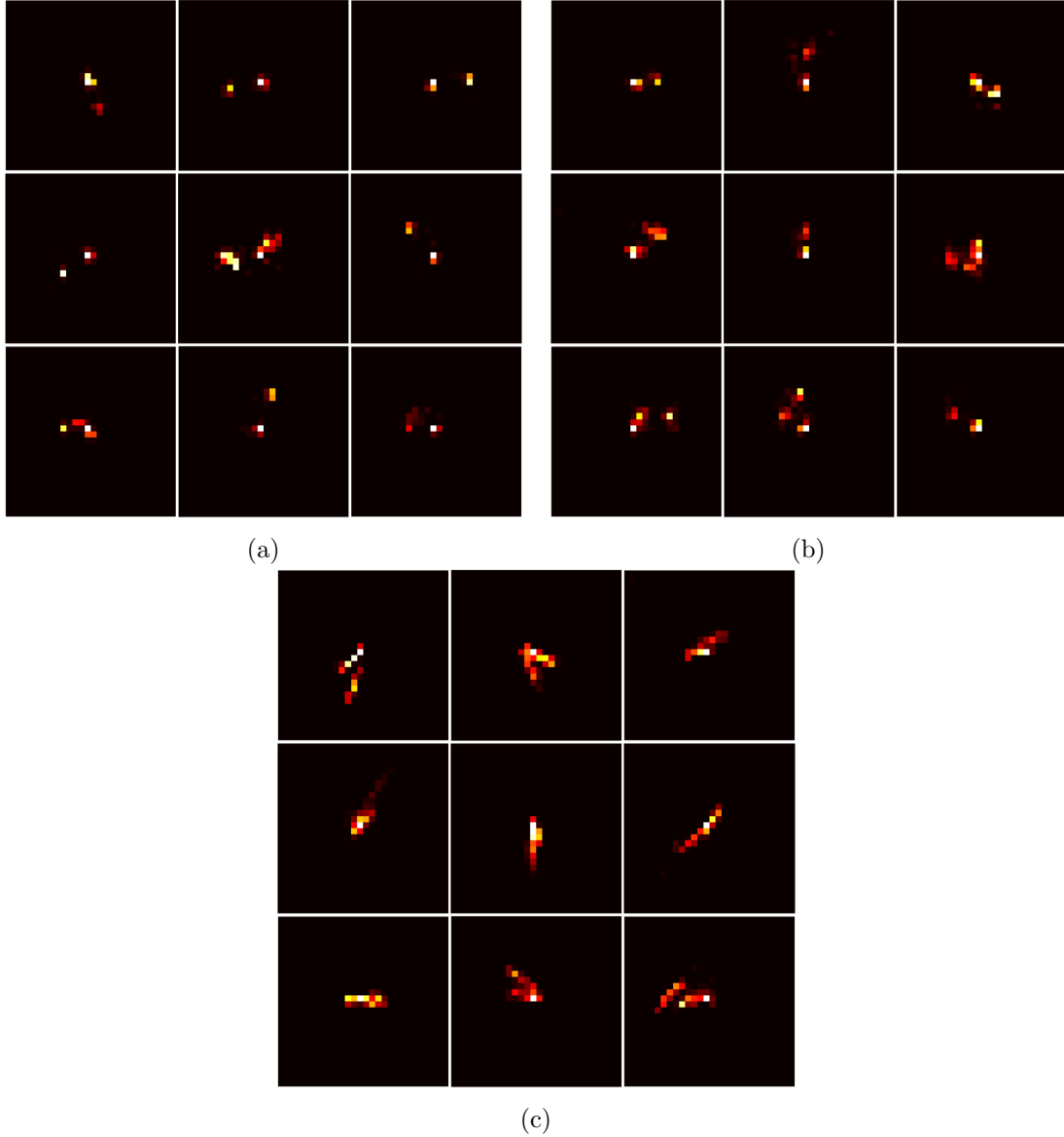


**Figure 5:** Typical energy deposition images of nine events from (a) non-displaced  $Z$ , (b)  $Z$  having a transverse displacement between 50 cm – 70 cm and (c)  $Z$  having a transverse displacement between 200 cm – 220 cm. With increasing displacement, energy deposition becomes more and more elongated.

Standard cut-based analyses, therefore, might not be effective for this study. Even in the distributions shown in Fig. 3, the difference is present but subtle (note that the plots are shown in log scale). This motivates us to look for other powerful alternatives that can identify these subtle features and discriminate on the basis of that. We use image recognition technique by employing a CNN to check if this task can be achieved.

Before moving to the analysis using CNN, we study the difference in energy deposition patterns for the second scenario where the jets come directly from decay of LLP  $X$ .

### 2.2.2 Displaced jets directly from LLP decay

For the second scenario, we consider the decay of a boosted LLP  $X$  into three quarks, giving multiple displaced jets coming from the LLP.

$$X \rightarrow jjj$$

To simulate this scenario we use R-parity violating (RPV) SUSY [60] where the neutralino is again the LLP and it can decay to three quarks via the  $\lambda''_{ijk}$  (UDD) coupling.

We use PYTHIA6 for generation of events and consider a non-displaced scenario along with the four cases with different displacements (list in section 2.2). Also, to ensure that the decay products fall mostly within the calorimeter segment, we put a condition that the longitudinal displacement is less than 200 cm and  $X$  is produced centrally ( $|\eta| < 0.7$ ). The mass of  $X$  is taken to be 100 GeV (close to SM  $Z$  boson mass to ensure that the multijet system here has similar boost as in the first scenario so that we can compare the two scenarios). We again take events where the HCAL energy deposit in  $28 \times 28$   $i\eta - i\phi$  plane is between (400, 500) GeV to make  $X$  boosted enough such that its decay products come closer in the  $\eta - \phi$  plane.

Fig. 6 shows the normalised distributions of energy fractions for different scenarios discussed above. We observe that the cases where the decay happens within the Tracker have some slight differences with increasing the displacement gradually as we have seen in the previous scenario (section 2.2.1). And the 200 cm – 220 cm displaced case is very different from the other cases. There most of the energy is contained within the central  $3 \times 3$  part of the  $i\eta - i\phi$  plane.

Fig. 7 shows the average of 50,000  $X \rightarrow jjj$  images for each of the four cases of decay within Tracker. Here, since we have not applied any preprocessing, we cannot make out the three separate jets in the average images. We observe that with displacement the energy deposit becomes more contained in smaller  $\eta - \phi$  region. As observed from the distributions in Fig. 6, for the maximum displaced case of 200 – 220 cm, most of the energy deposition is contained within the first  $3 \times 3$  block. The segmentation in the  $z$  direction corresponding to 0.1  $\eta$  segmentation gets bigger in physical size as one moves away from the IP radially (the segment size in  $z$  direction for  $\Delta\eta = 0.1$  radian increases from A to C layers as can be seen in Fig. 1). For the 200 – 220 cm displaced case, the decay happens just before entering the HCAL and therefore, the physical area taken by the decay products is very small and they mostly get contained within fewer  $\eta - \phi$  towers. This is another important feature that we observe for displaced energy depositions.

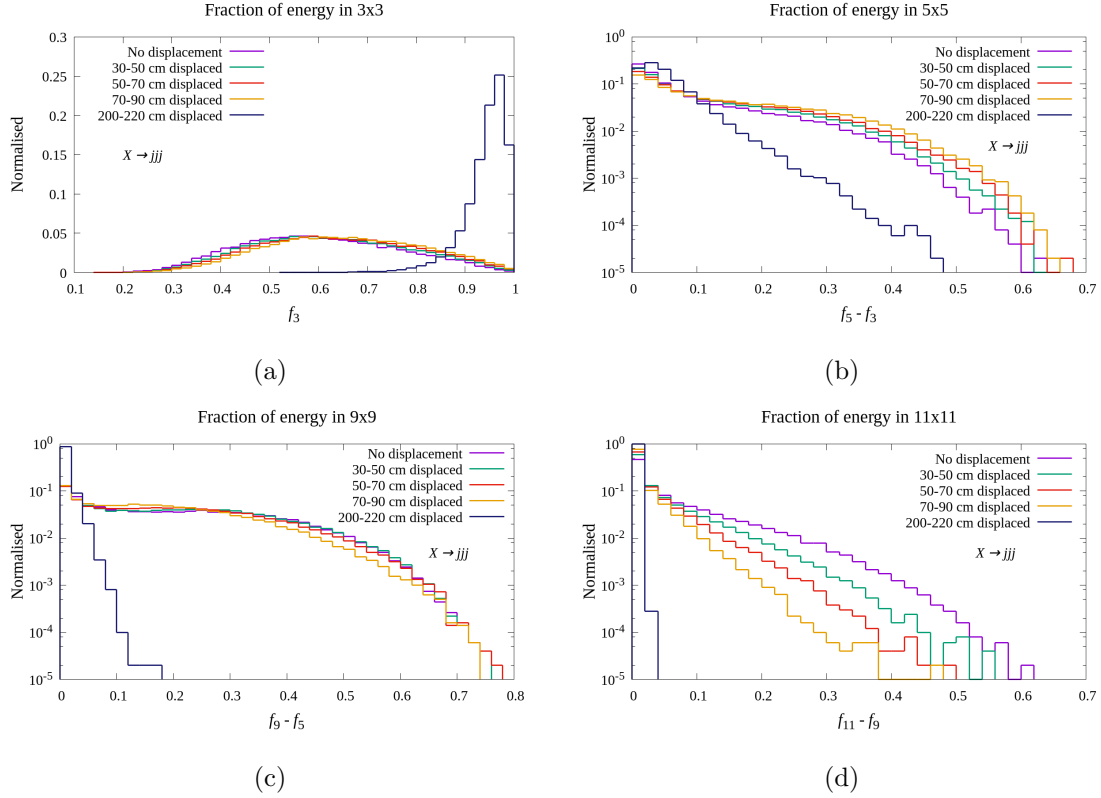


**Figure 6:** Normalised distributions of energy deposition fraction ( $f_i$ ) with varying sizes of blocks ( $i \times i$ ). (a) Fraction of energy deposited in  $3 \times 3$ ; (b),(c),(d) Fraction of energy deposited in  $5 \times 5$ ,  $9 \times 9$  and  $11 \times 11$  excluding the previous  $3 \times 3$ ,  $5 \times 5$  and  $9 \times 9$  blocks' energy deposition fraction respectively.

This effect was also present in the displaced  $Z$  case. It's more prominent for this case because here the  $X$  is centrally produced and jets are coming directly from the decay of a boosted  $X$  and are therefore, more collimated. So here, there is not much mismatch between the displaced particles'  $\eta - \phi$  and the standard calorimeter segments. Therefore, the elongation of each objects' energy deposition is very little and the energy deposition of the multijet system is more contained. For the previous case, the displaced jets come from the displaced  $Z$  and even if the LLP  $X$  is centrally produced,  $Z$ 's  $\eta$  can have many possible values giving us more chances of mismatch with standard calorimeter segments, and hence the elongation feature is more.

To summarise the last two sections (2.2.1 and 2.2.2), we identify two important features associated with displaced multijet systems. They are –

- **Elongated energy deposits in the HCAL**

This happens due to the mismatch of displaced particles'  $\eta - \phi$  direction with standard calorimeter  $\eta - \phi$  towers. Therefore, energy deposition of displaced jets in the HCAL have more elongated patterns which differ from standard patterns of prompt jets.

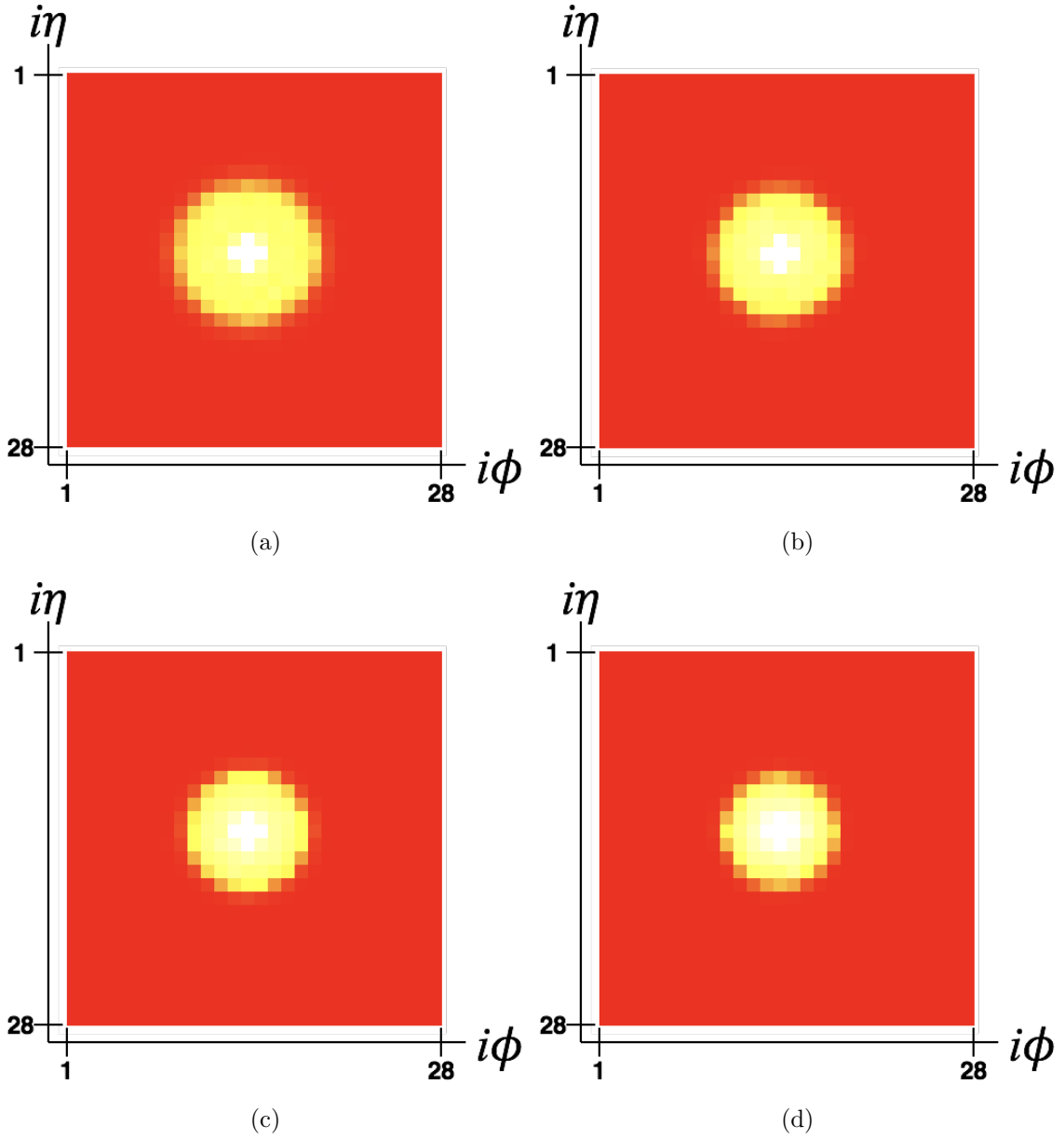


**Figure 7:** Average of 50,000 images for (a) prompt jets from  $X$ ; (b),(c),(d) jets displaced within 30 – 50 cm, 50 – 70 cm and 70 – 90 cm transverse distance from PV respectively. These are  $28 \times 28$  images in the  $i\eta - i\phi$  plane with the highest energy bin in the center (14,14). With increasing displacement, the energy deposition is contained to smaller  $i\eta - i\phi$  region.

- **Total energy deposit of the multijet system more contained in the  $i\eta - i\phi$  region**

The jets coming from the decay of the LLP have some  $\Delta R$ <sup>6</sup> between them. If the

---

<sup>6</sup> $\Delta R = \sqrt{\Delta\eta^2 + \Delta\phi^2}$

jets from  $X$  have the same  $\Delta R$  in both prompt decay as well as late decay of  $X$ , the energy deposit is smaller for the displaced case because the physical segmentation of the detector (in  $z$  direction) has increased with increasing radial distance.

The above features give different energy deposition patterns at the HCAL but the difference for displaced and non-displaced cases are not significant enough at the level of individual events so that we can use the usual cut-based analysis to discriminate them. We therefore use the HCAL energy deposition images to train a convolutional neural network to learn these displaced features and discriminate displaced cases from prompt cases on the basis of that for both the LLP scenarios.

### 2.3 The Convolution Neural Network

The Convolutional Neural Network (CNN) [61] is one of the most notable deep learning approaches used in diverse computer vision applications. We use Tensorflow[62] for implementing the CNN used in this work for discriminating displaced objects from non-displaced standard objects in the collider. As described in section 2.1, we have  $28 \times 28$  images of HCAL energy deposition for all scenarios. These images are the input of our neural network. We now briefly discuss the various components of the network.

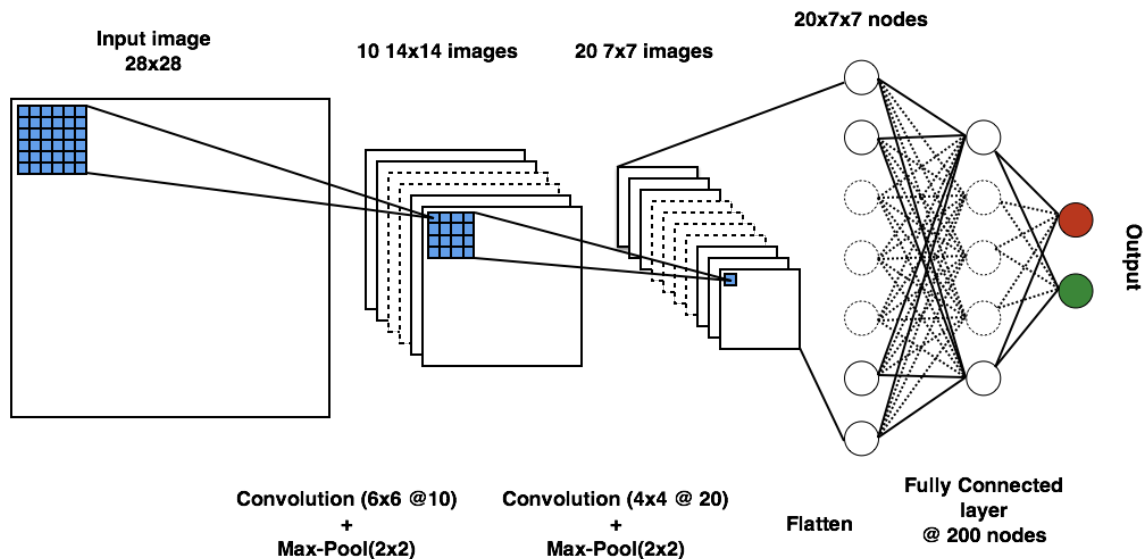


Figure 8: The CNN architecture used.

#### 2.3.1 Network Architecture

1. **Convolution Layer:** In convolutional layers, the algorithm utilises various kernels to convolve the whole image to generate various feature maps. We use two convolution layers: Layer 1: 10 filters of kernel size  $6 \times 6$ ; and Layer 2: 20 filters of kernel size  $4 \times 4$ , with a stride of  $1 \times 1$  for both the layers, which means that the filter convolves around the input volume by shifting one unit at a time. The objective of the convolution operation is to extract features such as edges and shapes. In order to introduce



nonlinearity to the system, activation function of Rectified Linear Unit (RELU)[63] has been applied to the outputs; and L2 regularization [64] has been applied to the kernel weights. The outputs of the convolution layer are also batch normalised[65].

2. **Max-Pool:** After each convolution layer, the output has been max-pooled with a pool size of  $2 \times 2$  which means that each  $2 \times 2$  kernel of the convolution output has been replaced by the maximum value in that kernel. This reduces the dimension of the image by half after each max-pooling and finally we have  $20 \times 7 \times 7$  images after convolution and max-pooling. By now, we have enabled the model to understand the features. Next, we will flatten the output and feed it to a regular Neural Network for classification purposes.
3. **Flatten and Fully Connected (FC) Layer:** At this stage, we flatten these images and get  $20 \times 7 \times 7$ , i.e., 980 input values which we connect to a fully connected layer with 200 nodes. Activation function RELU is applied. We apply a 50% dropout[66] to this FC layer to deal with the problem of overfitting. Finally this layer is connected to the binary output through a softmax activation function [67].

Fig. 8 summarises the network architect used in this work. We use Adam Optimizer[68] with a learning rate of 0.001. We train to minimise the cross-entropy loss function [69]. We have done some naive optimisations to decide on the present network architecture and hyperparameters.

### 2.3.2 Dataset

We have used 100,000 images (including both classes) out of which 60,000 images have been used for training, 20,000 for validation and another 20,000 for testing the network. We use a batch size of 200 while training. The training was stopped at the epoch with minimum validation loss when this loss was not decreasing significantly.

We performed the classification between the non-displaced case and the four different displaced cases for each of the two scenarios – displaced  $Z$  from  $X$  which decays to jets and displaced jets coming from  $X$  directly.

## 2.4 Analysis and Results

For analysing the performance of the network, we draw a Receiver Operating Characteristics (ROC)[70] curve with signal efficiency vs. background rejection. Since we want to study the difference in energy deposition patterns as a result of displacement of particles, here, we consider the non-displaced events as our background and the four displaced cases as separate signals. We use the test output of the CNN to draw the ROC curves. These curves will give us an idea of the discriminating power of the classifier for different displacements and for which signal, it works the best.

### 2.4.1 Displaced jets from displaced $Z$

Fig. 9 shows the ROCs of the CNN performance for the non-displaced vs the four cases with different displacements of  $Z$  boson.

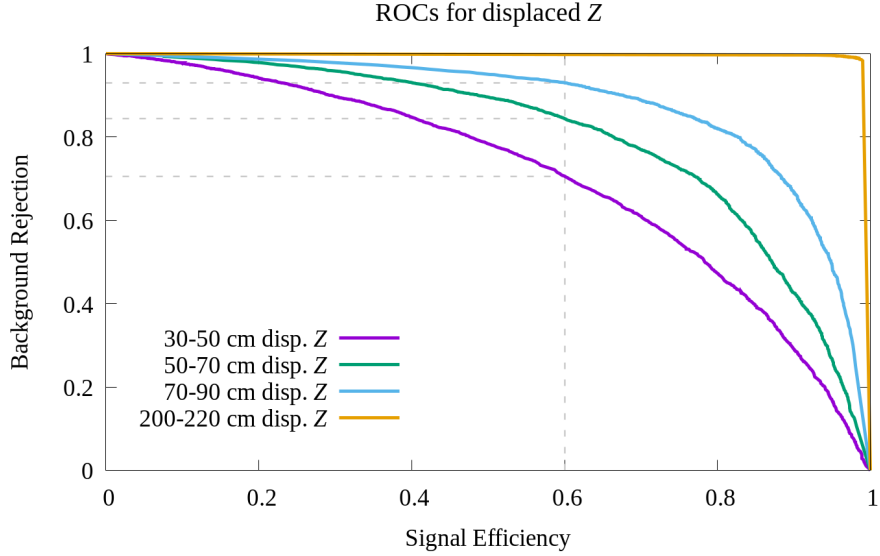


**Figure 9:** ROCs of the CNN performance to separate non-displaced  $Z$  from different classes of displaced  $Z$ .

We get background rejection of 70.61%, 84.36% and 93.02% for a signal efficiency of 60% for 30 cm–50 cm displaced  $Z$ , 50 cm–70 cm displaced  $Z$ , and 70 cm–90 cm displaced  $Z$  respectively. We notice that the performance of the network is better for more displaced  $Z$  which is expected. For the 200 cm – 220 cm displaced  $Z$ , the network performs the best. This implies that the network has learned the features associated with displacement and discriminates on the basis of that. For the most displaced case, there is more mismatch between the decay products  $\eta - \phi$  with the standard  $\eta - \phi$  HCAL towers, hence more elongated energy deposition in the HCAL. We therefore find that this analysis is better for more displaced scenarios, where usually our standard reconstructions fail badly.

In the above analysis the mass of  $X$  was taken to be 800 GeV. We now study the dependence of this analysis on mass of the LLP. We consider the performance of the network to discriminate 70 – 90 cm displaced  $Z$  from prompt  $Z$  for three different masses of  $X$  – 500 GeV, 800 GeV and 1500 GeV. We choose the same energy window cut (400, 500) GeV for all these cases. Hence, the boost of the multijet system coming from  $Z$  remains the same for all the cases. Fig. 10 shows the ROCs for the CNN performance to separate non-displaced  $Z$  from 70 cm – 90 cm displaced  $Z$  for these different  $X$  masses. We find that with increasing  $X$  mass the CNN performs better, although the effect is not drastic.

Massive LLPs travel slower in the detector and therefore their decay products can have large  $\Delta R$  between them. Large  $\Delta R$  between the  $Z$  and the invisible particle means that the jets from  $Z$  pass through different standard  $\eta - \phi$  calorimeter towers in different layers and hence the projection along constant  $\eta - \phi$  of these radial layers will have more elongated energy deposition pattern. This improves the discrimination power of the CNN with increasing LLP mass.

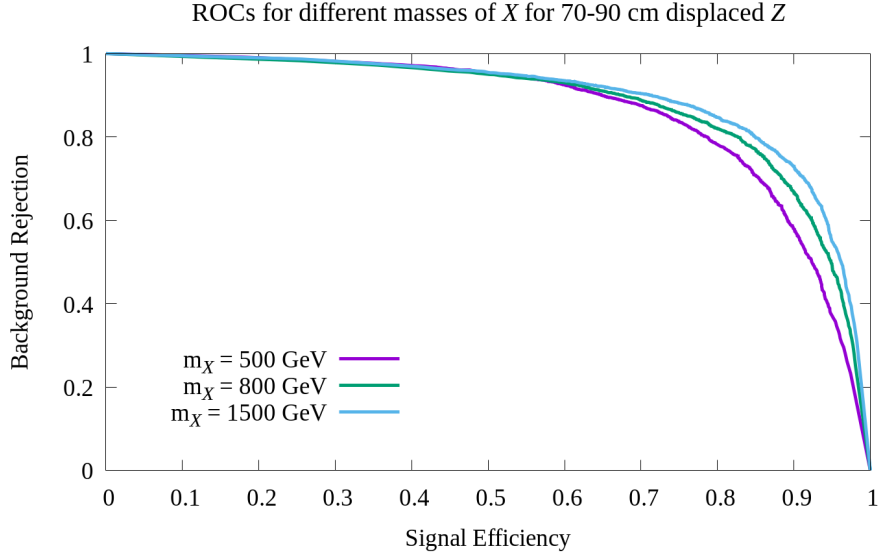


**Figure 10:** ROCs of the CNN performance to separate non-displaced  $Z$  from 70 cm–90 cm displaced  $Z$  for different masses of  $X$ .

#### 2.4.2 Displaced jets directly from LLP decay

Fig. 11 shows the ROCs of the CNN performance for the non-displaced vs the four cases with different displacements of the jets coming from the decay of  $X$ .

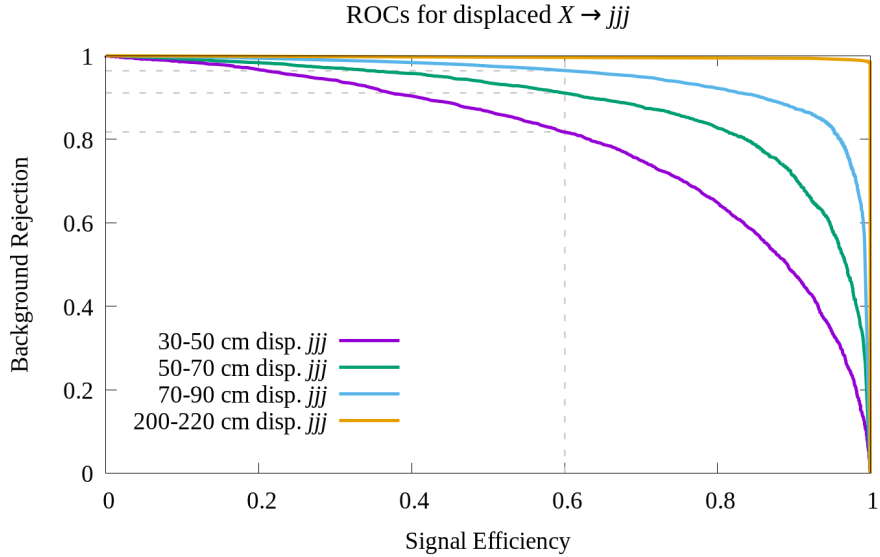


**Figure 11:** ROCs of the CNN performance to separate non-displaced  $jjj$  from different classes of displaced  $jjj$ .

We get background rejection of 81.70%, 91.06% and 96.39% for a signal efficiency of 60% for 30 cm – 50 cm displaced, 50 cm – 70 cm displaced, and 70 cm – 90 cm displaced

decay of  $X$  respectively. Again the performance of the network is better for more displaced cases, being the best for the 200 cm – 220 cm displaced decay of  $X$ .

Varying the mass of the LLP in this scenario needs different energy deposition window cut (other than (400, 500) GeV) for giving the same amount of boost to the final multijet system. We believe that if the multijet system has the same boost, the results won't be affected with variation of LLP mass for this scenario.

Therefore, we find that CNNs can learn displaced features from HCAL energy <sup>7</sup> deposition images and is able to discriminate prompt multijet systems from displaced ones. The two scenarios considered by us had some kinematic differences. Yet the network performs equally well for both the scenarios with increasing displacement. This suggests that this kind of analysis is quite robust to the LLP model that we consider and hence can be extended to study other LLP decaying to multijet scenarios as well.

We end this section with a brief discussion of a special case of  $X \rightarrow jjj$  where  $X$  decays at rest. This resembles the case of a color neutral R-hadron stopping in the detector and decaying into jets. We study whether HCAL images have any potential for stopped R-hadron studies.

### Stopped particle scenario

Particles with longer lifetime can occur in split supersymmetry [7], where the decay of gluino ( $\tilde{g}$ ) is suppressed due to the large mass difference between gluino and squark; i.e. squark is much heavier than gluino in this model. If long-lived gluinos exist they might be produced in the  $pp$  collisions in the LHC, and they will soon hadronise to make a hadron-like state, generally referred to as R-hadrons. These R-hadron can be charged or neutral, and they will lose energy by interacting with the material of the detector as they travel through it. For heavy R-hadrons, which will move slowly, the energy loss will be sufficient to stop a significant fraction of the produced R-hadrons inside the calorimeter of the detector. These stopped particles may decay seconds, minutes, hours, or days later, resulting in out-of-time energy deposits in the calorimeter [71].

We want to explore how the HCAL energy deposition pattern would look like for a stopped particle scenario. We expect this to be quite different from standard deposition patterns. Since the stopped particle decays at rest at a significant distance from the PV,  $\eta$  and  $\phi$  of the decay products don't match with the HCAL  $\eta - \phi$  segmentation. The energy deposit of these particles, therefore, won't be contained in one or two  $\eta - \phi$  towers of the HCAL. We rather expect these energy deposits to look like lines on the  $\eta - \phi$  plane.

To demonstrate this, we consider the decay of  $X$  of mass 1 TeV to three quarks as described for the second scenario above. We use PYTHIA6 and RPV SUSY model to simulate this case. But here the LLP  $X$  is made to decay at rest. The position where  $X$  stops is simulated such that it follows an exponential distribution. We consider events where  $X$  has stopped in the first HCAL layer. After  $X$  decays, we will get some particles moving in the forward direction as well as some in the backward direction to conserve momentum. The

---

<sup>7</sup>We have repeated this analysis by also considering images of transverse energy deposition in the HCAL. Our results are robust against this change.

backward moving particles have very unique signatures in the collider and is in itself a very interesting subject of study [72]. In the present work, we only consider the energy deposition of forward-moving particles. Therefore, most of the events have energy deposition in the HCAL between (400, 500) GeV, which is about half of the  $X$  mass.

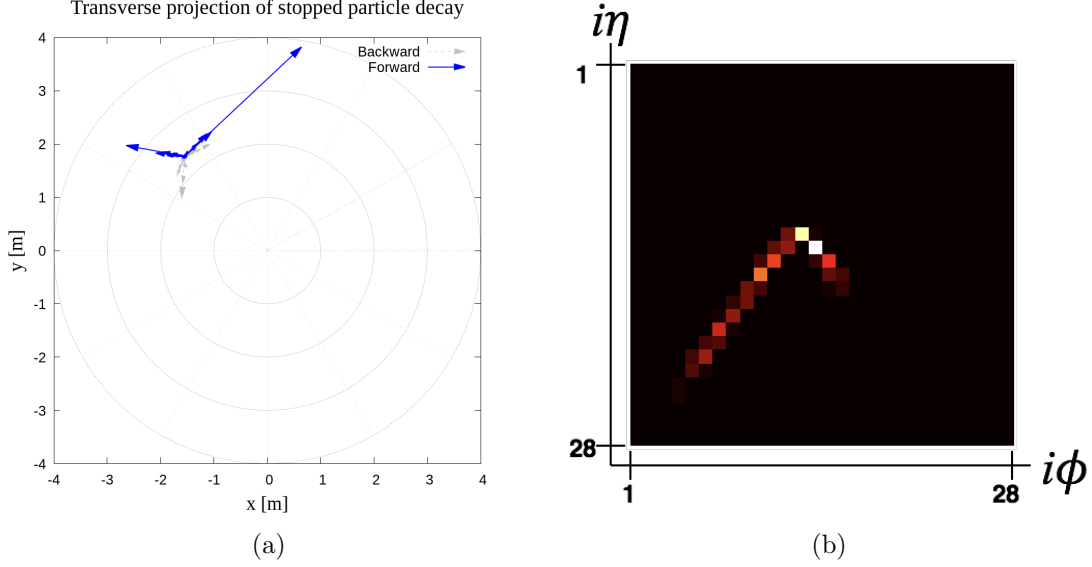


**Figure 12:** (a) Stopped particle decay projection in the transverse plane – shown in grey and blue are particles moving backward and forward respectively; (b) Energy deposition of forward-moving particles coming from the decay of a stopped particle in the HCAL. Both images are for the same stopped particle decay event.

Fig. 12a shows the  $x$ - $y$  (transverse) projection of a typical stopped  $X$  decay. Marked in blue are the particles moving in the forward direction which we have propagated through our segmented HCAL. Fig. 12b shows the energy deposit of forward-moving particles for the same event in  $i\eta$ - $i\phi$  plane. We find that this energy deposition pattern is quite different from standard scenarios. Inclusion of backward-moving particles will enhance this feature and we will get more such lines.

Since top quarks can decay to three quarks, we have performed a classification between stopped  $X$  decaying to three jets and top quark using the CNN architect as described in section 2.3 with energy of top lying between (400, 500) GeV, same as the energy range for stopped case. They have very different energy deposition patterns in the HCAL and as expected we get high accuracy from the CNN training as well as validation. Even for 95% stopped particle tagging efficiency, we get  $\sim 99\%$  single top background rejection efficiency.

The significantly different energy deposition pattern of the stopped particles in the HCAL indicates that one need not wait for empty bunch-crossings at colliders to search for stopped R-hadrons. Instead these HCAL energy deposition images of stopped particles can serve as important tools for their searches.

### 3 Conclusion and Outlook

This work presents an idea of how HCAL images along with image recognition techniques can be used in the search for long-lived particles. To the best of our knowledge, this work is the first attempt in studying LLPs using energy deposition images and image recognition techniques. LLPs are difficult to identify using standard reconstructions due to their displacement from the PV. In this work we consider two scenarios which are different in the sense that in one, the displaced jets come from the decay of an intermediate displaced SM particle ( $Z$  boson) while in the other they directly come from the decay of the LLP. By studying the energy deposition patterns of LLPs with varying displacements, in these two scenarios, we observe two key features. One is, elongation in energy deposition because  $\eta$  and  $\phi$  of particles which are very much displaced from the PV do not match with standard detector  $\eta - \phi$  segmentation. Another one is, later the decay of the LLP, smaller is the physical region in which the energy deposition of its decay products is contained in HCAL. Due to the absence of layered structure and  $z$  segmentation in fast detector simulations like `Delphes`, we can't use them to study these features for displaced jets. Therefore, we simulate our simplified calorimeter following the segmentation of the Tile Calorimeter of ATLAS.

We used these displaced features of LLPs that give different energy deposition patterns in the HCAL to differentiate them from non-displaced objects using a convolutional neural network. Our analysis performs better for LLPs which decay at larger distances from the PV, where usual displaced jets analysis might lose sensitivity due to failure of standard reconstructions. Therefore, this might serve as a complementary analysis to standard LLP analyses.

As a limiting case of the second scenario where the jets come directly from the LLP decay, we consider the situation where the LLP stops before decaying. We show that stopped particles also have very different energy deposition patterns in the calorimeter. Therefore, we can consider to look for such HCAL images rather than waiting for empty bunch crossings for the search of stopped R-hadrons.

We have used minimal preprocessing to the images and have not done advanced optimisations. We would like to reiterate here that the major focus of this study was to show the feasibility of probing displaced jets emanating from the decay of an LLP via ML techniques. Advanced pre-processing and optimisations can be done for dedicated LLP searches.

Although we have shown this image-based analysis technique for some particular scenarios in this work, we believe that it will work for any scenario where an LLP decays into multiple jets. Therefore, this can be treated as a robust search technique for LLPs decaying to give displaced jets in the final state. This work is a simple-minded analysis done for the proof-of-principle that displaced jets have some different energy deposition features and these can be identified using an image based study.

*Acknowledgements:* The work of B.B. is supported by the Department of Science and Technology, Government of India, under Grant No. IFA13- PH-75 (INSPIRE Faculty

Award). The work of S.M. is supported by the German Federal Ministry of Education and Research BMBF. R.S. would like to thank Rahool Kumar Barman and Amit Adhikary for useful discussions.

## References

- [1] M. J. Strassler and K. M. Zurek, “Echoes of a hidden valley at hadron colliders,” *Phys. Lett. B* **651**, 374 (2007) doi:10.1016/j.physletb.2007.06.055 [hep-ph/0604261].
- [2] D. Curtin, R. Essig, S. Gori and J. Shelton, “Illuminating Dark Photons with High-Energy Colliders,” *JHEP* **1502**, 157 (2015) doi:10.1007/JHEP02(2015)157 [arXiv:1412.0018 [hep-ph]].
- [3] J. Liu, Z. Liu and L. T. Wang, *Phys. Rev. Lett.* **122**, no. 13, 131801 (2019) doi:10.1103/PhysRevLett.122.131801 [arXiv:1805.05957 [hep-ph]].
- [4] R. Kumar Barman, B. Bhattacharjee, A. Chatterjee, A. Choudhury and A. Gupta, “Scope of strongly self-interacting thermal WIMPs in a minimal  $U(1)_D$  extension and its future prospects,” arXiv:1811.09195 [hep-ph].
- [5] S. Alipour-Fard, N. Craig, M. Jiang and S. Koren, arXiv:1812.05588 [hep-ph].
- [6] G. F. Giudice and R. Rattazzi, *Phys. Rept.* **322**, 419 (1999) doi:10.1016/S0370-1573(99)00042-3 [hep-ph/9801271].
- [7] J. L. Hewett, B. Lillie, M. Masip and T. G. Rizzo, “Signatures of long-lived gluinos in split supersymmetry,” *JHEP* **0409**, 070 (2004) doi:10.1088/1126-6708/2004/09/070 [hep-ph/0408248].
- [8] P. Meade, M. Reece and D. Shih, *JHEP* **1010**, 067 (2010) doi:10.1007/JHEP10(2010)067 [arXiv:1006.4575 [hep-ph]].
- [9] J. Fan, M. Reece and J. T. Ruderman, “A Stealth Supersymmetry Sampler,” *JHEP* **1207**, 196 (2012) doi:10.1007/JHEP07(2012)196 [arXiv:1201.4875 [hep-ph]].
- [10] B. Bhattacharjee, B. Feldstein, M. Ibe, S. Matsumoto and T. T. Yanagida, *Phys. Rev. D* **87**, no. 1, 015028 (2013) doi:10.1103/PhysRevD.87.015028 [arXiv:1207.5453 [hep-ph]].
- [11] A. Arvanitaki, N. Craig, S. Dimopoulos and G. Villadoro, *JHEP* **1302**, 126 (2013) doi:10.1007/JHEP02(2013)126 [arXiv:1210.0555 [hep-ph]].
- [12] S. Banerjee, G. Blanger, B. Mukhopadhyaya and P. D. Serpico, *JHEP* **1607**, 095 (2016) doi:10.1007/JHEP07(2016)095 [arXiv:1603.08834 [hep-ph]].
- [13] N. Nagata, H. Otono and S. Shirai, *JHEP* **1703**, 025 (2017) doi:10.1007/JHEP03(2017)025 [arXiv:1701.07664 [hep-ph]].
- [14] S. Banerjee, G. Blanger, A. Ghosh and B. Mukhopadhyaya, *JHEP* **1809**, 143 (2018) doi:10.1007/JHEP09(2018)143 [arXiv:1806.04488 [hep-ph]].
- [15] H. Ito, O. Jinnouchi, T. Moroi, N. Nagata and H. Otono, *JHEP* **1806**, 112 (2018) doi:10.1007/JHEP06(2018)112 [arXiv:1803.00234 [hep-ph]].
- [16] Y. Cui and B. Shuve, “Probing Baryogenesis with Displaced Vertices at the LHC,” *JHEP* **1502**, 049 (2015) doi:10.1007/JHEP02(2015)049 [arXiv:1409.6729 [hep-ph]].
- [17] K. Y. Choi, S. K. Kang and J. Kim, “Non-thermal WIMP baryogenesis,” *Phys. Lett. B* **782**, 657 (2018) doi:10.1016/j.physletb.2018.05.083 [arXiv:1803.00820 [hep-ph]].



- [18] R. N. Mohapatra and J. C. Pati, “A Natural Left-Right Symmetry,” *Phys. Rev. D* **11**, 2558 (1975). doi:10.1103/PhysRevD.11.2558.
- [19] P. S. B. Dev, R. N. Mohapatra and Y. Zhang, “Long Lived Light Scalars as Probe of Low Scale Seesaw Models,” *Nucl. Phys. B* **923**, 179 (2017) doi:10.1016/j.nuclphysb.2017.07.021 [arXiv:1703.02471 [hep-ph]].
- [20] G. Cottin, J. C. Helo and M. Hirsch, “Searches for light sterile neutrinos with multitrack displaced vertices,” *Phys. Rev. D* **97**, no. 5, 055025 (2018) doi:10.1103/PhysRevD.97.055025 [arXiv:1801.02734 [hep-ph]].
- [21] P. S. Bhupal Dev and Y. Zhang, “Displaced vertex signatures of doubly charged scalars in the type-II seesaw and its left-right extensions,” *JHEP* **1810**, 199 (2018) doi:10.1007/JHEP10(2018)199 [arXiv:1808.00943 [hep-ph]].
- [22] A. M. Sirunyan *et al.* [CMS Collaboration], “Search for long-lived particles decaying into displaced jets in proton-proton collisions at  $\sqrt{s} = 13$  TeV,” *Phys. Rev. D* **99**, no. 3, 032011 (2019) doi:10.1103/PhysRevD.99.032011 [arXiv:1811.07991 [hep-ex]].
- [23] A. M. Sirunyan *et al.* [CMS Collaboration], “Search for new particles decaying to a jet and an emerging jet,” *JHEP* **1902**, 179 (2019) doi:10.1007/JHEP02(2019)179 [arXiv:1810.10069 [hep-ex]].
- [24] A. M. Sirunyan *et al.* [CMS Collaboration], “Search for long-lived particles with displaced vertices in multijet events in proton-proton collisions at  $\sqrt{s} = 13$  TeV,” *Phys. Rev. D* **98**, no. 9, 092011 (2018) doi:10.1103/PhysRevD.98.092011 [arXiv:1808.03078 [hep-ex]].
- [25] A. M. Sirunyan *et al.* [CMS Collaboration], “Search for decays of stopped exotic long-lived particles produced in proton-proton collisions at  $\sqrt{s} = 13$  TeV,” *JHEP* **1805**, 127 (2018) doi:10.1007/JHEP05(2018)127 [arXiv:1801.00359 [hep-ex]].
- [26] A. M. Sirunyan *et al.* [CMS Collaboration], “Search for disappearing tracks as a signature of new long-lived particles in proton-proton collisions at  $\sqrt{s} = 13$  TeV,” *JHEP* **1808**, 016 (2018) doi:10.1007/JHEP08(2018)016 [arXiv:1804.07321 [hep-ex]].
- [27] M. Aaboud *et al.* [ATLAS Collaboration], “Search for long-lived neutral particles in  $pp$  collisions at  $\sqrt{s} = 13$  TeV that decay into displaced hadronic jets in the ATLAS calorimeter,” arXiv:1902.03094 [hep-ex].
- [28] M. Aaboud *et al.* [ATLAS Collaboration], “Search for heavy charged long-lived particles in the ATLAS detector in 31.6 fb<sup>-1</sup> of proton-proton collision data at  $\sqrt{s} = 13$  TeV,” arXiv:1902.01636 [hep-ex].
- [29] M. Aaboud *et al.* [ATLAS Collaboration], “Search for heavy long-lived multicharged particles in proton-proton collisions at  $\sqrt{s} = 13$  TeV using the ATLAS detector,” *Phys. Rev. D* **99**, no. 5, 052003 (2019) doi:10.1103/PhysRevD.99.052003 [arXiv:1812.03673 [hep-ex]].
- [30] M. Aaboud *et al.* [ATLAS Collaboration], “Search for long-lived particles produced in  $pp$  collisions at  $\sqrt{s} = 13$  TeV that decay into displaced hadronic jets in the ATLAS muon spectrometer,” *Phys. Rev. D* **99**, no. 5, 052005 (2019) doi:10.1103/PhysRevD.99.052005 [arXiv:1811.07370 [hep-ex]].
- [31] M. Aaboud *et al.* [ATLAS Collaboration], “Search for the production of a long-lived neutral particle decaying within the ATLAS hadronic calorimeter in association with a  $Z$  boson from  $pp$  collisions at  $\sqrt{s} = 13$  TeV,” Submitted to: *Phys.Rev.Lett.* [arXiv:1811.02542 [hep-ex]].

- [32] R. Aaij *et al.* [LHCb Collaboration], “Updated search for long-lived particles decaying to jet pairs,” *Eur. Phys. J. C* **77**, no. 12, 812 (2017) doi:10.1140/epjc/s10052-017-5178-x [arXiv:1705.07332 [hep-ex]].
- [33] R. Aaij *et al.* [LHCb Collaboration], “Search for massive long-lived particles decaying semileptonically in the LHCb detector,” *Eur. Phys. J. C* **77**, no. 4, 224 (2017) doi:10.1140/epjc/s10052-017-4744-6 [arXiv:1612.00945 [hep-ex]].
- [34] J. Alimena *et al.*, “Searching for long-lived particles beyond the Standard Model at the Large Hadron Collider,” arXiv:1903.04497 [hep-ex].
- [35] S. Chatrchyan *et al.* [CMS Collaboration], “Search for long-lived particles decaying to photons and missing energy in proton-proton collisions at  $\sqrt{s} = 7$  TeV,” *Phys. Lett. B* **722**, 273 (2013) doi:10.1016/j.physletb.2013.04.027 [arXiv:1212.1838 [hep-ex]].
- [36] K. Albertsson *et al.*, “Machine Learning in High Energy Physics Community White Paper,” *J. Phys. Conf. Ser.* **1085**, no. 2, 022008 (2018) doi:10.1088/1742-6596/1085/2/022008 [arXiv:1807.02876 [physics.comp-ph]].
- [37] P. Adamson *et al.* [NOvA Collaboration], “Search for active-sterile neutrino mixing using neutral-current interactions in NOvA,” *Phys. Rev. D* **96**, no. 7, 072006 (2017) doi:10.1103/PhysRevD.96.072006 [arXiv:1706.04592 [hep-ex]].
- [38] R. Acciarri *et al.* [MicroBooNE Collaboration], “Convolutional Neural Networks Applied to Neutrino Events in a Liquid Argon Time Projection Chamber,” *JINST* **12**, no. 03, P03011 (2017) doi:10.1088/1748-0221/12/03/P03011 [arXiv:1611.05531 [physics.ins-det]].
- [39] L. de Oliveira, M. Kagan, L. Mackey, B. Nachman and A. Schwartzman, “Jet-images deep learning edition,” *JHEP* **1607**, 069 (2016) doi:10.1007/JHEP07(2016)069 [arXiv:1511.05190 [hep-ph]].
- [40] J. Cogan, M. Kagan, E. Strauss and A. Schwartzman, “Jet-Images: Computer Vision Inspired Techniques for Jet Tagging,” *JHEP* **1502**, 118 (2015) doi:10.1007/JHEP02(2015)118 [arXiv:1407.5675 [hep-ph]].
- [41] A. J. Larkoski, I. Moult and B. Nachman, “Jet Substructure at the Large Hadron Collider: A Review of Recent Advances in Theory and Machine Learning,” arXiv:1709.04464 [hep-ph].
- [42] J. Pearkes, W. Fedorko, A. Lister and C. Gay, “Jet Constituents for Deep Neural Network Based Top Quark Tagging,” arXiv:1704.02124 [hep-ex].
- [43] L. G. Almeida, M. Backovi, M. Cliche, S. J. Lee and M. Perelstein, “Playing Tag with ANN: Boosted Top Identification with Pattern Recognition,” *JHEP* **1507**, 086 (2015) doi:10.1007/JHEP07(2015)086 [arXiv:1501.05968 [hep-ph]].
- [44] G. Kasieczka, T. Plehn, M. Russell and T. Schell, “Deep-learning Top Taggers or The End of QCD?,” *JHEP* **1705**, 006 (2017) doi:10.1007/JHEP05(2017)006 [arXiv:1701.08784 [hep-ph]].
- [45] G. Kasieczka *et al.*, “The Machine Learning Landscape of Top Taggers,” arXiv:1902.09914 [hep-ph].
- [46] J. A. Aguilar-Saavedra, J. H. Collins and R. K. Mishra, “A generic anti-QCD jet tagger,” *JHEP* **1711**, 163 (2017) doi:10.1007/JHEP11(2017)163 [arXiv:1709.01087 [hep-ph]].
- [47] T. S. Roy and A. H. Vijay, “A robust anomaly finder based on autoencoder,” arXiv:1903.02032 [hep-ph].

- [48] S. Ghosh, A. Harilal, A. R. Sahasransu, R. K. Singh and S. Bhattacharya, “A simulation study to distinguish prompt photon from  $\pi^0$  and beam halo in a granular calorimeter using deep networks,” JINST **14**, no. 01, P01011 (2019) doi:10.1088/1748-0221/14/01/P01011 [arXiv:1808.03987 [physics.ins-det]].
- [49] D. Guest, J. Collado, P. Baldi, S. C. Hsu, G. Urban and D. Whiteson, “Jet Flavor Classification in High-Energy Physics with Deep Neural Networks,” Phys. Rev. D **94**, no. 11, 112002 (2016) doi:10.1103/PhysRevD.94.112002 [arXiv:1607.08633 [hep-ex]].
- [50] M. Farina, Y. Nakai and D. Shih, “Searching for New Physics with Deep Autoencoders,” arXiv:1808.08992 [hep-ph].
- [51] A. Chakraborty, S. H. Lim and M. M. Nojiri, “Interpretable Deep Learning for Two-Prong Jet Classification with Jet Spectra,” arXiv:1904.02092 [hep-ph].
- [52] J. Hajer, Y. Y. Li, T. Liu and H. Wang, “Novelty Detection Meets Collider Physics,” arXiv:1807.10261 [hep-ph].
- [53] T. Heimel, G. Kasieczka, T. Plehn and J. M. Thompson, “QCD or What?,” SciPost Phys. **6**, 030 (2019) doi:10.21468/SciPostPhys.6.3.030 [arXiv:1808.08979 [hep-ph]].
- [54] O. Cerri, T. Q. Nguyen, M. Pierini, M. Spiropulu and J. R. Vlimant, “Variational Autoencoders for New Physics Mining at the Large Hadron Collider,” arXiv:1811.10276 [hep-ex].
- [55] J. H. Collins, K. Howe and B. Nachman, “Extending the search for new resonances with machine learning,” Phys. Rev. D **99**, no. 1, 014038 (2019) doi:10.1103/PhysRevD.99.014038 [arXiv:1902.02634 [hep-ph]].
- [56] G. Aad *et al.* [ATLAS Collaboration], “Readiness of the ATLAS Tile Calorimeter for LHC collisions,” Eur. Phys. J. C **70**, 1193 (2010) doi:10.1140/epjc/s10052-010-1508-y [arXiv:1007.5423 [physics.ins-det]].
- [57] J. de Favereau *et al.* [DELPHES 3 Collaboration], “DELPHES 3, A modular framework for fast simulation of a generic collider experiment,” JHEP **1402** (2014) 057 doi:10.1007/JHEP02(2014)057 [arXiv:1307.6346 [hep-ex]].
- [58] C. F. Kolda, “Gauge mediated supersymmetry breaking: Introduction, review and update,” Nucl. Phys. Proc. Suppl. **62**, 266 (1998) doi:10.1016/S0920-5632(97)00667-1 [hep-ph/9707450].
- [59] T. Sjostrand, P. Eden, C. Friberg, L. Lonnblad, G. Miu, S. Mrenna and E. Norrbin, “High-energy physics event generation with PYTHIA 6.1,” Comput. Phys. Commun. **135**, 238 (2001) doi:10.1016/S0010-4655(00)00236-8 [hep-ph/0010017].
- [60] R. Barbier *et al.*, “R-parity violating supersymmetry,” Phys. Rept. **420**, 1 (2005) doi:10.1016/j.physrep.2005.08.006 [hep-ph/0406039].
- [61] Y. Lecun, L. Bottou, Y. Bengio and P. Haffner, “Gradient-Based Learning Applied to Document Recognition,” doi:10.1109/5.726791, Proceedings of the IEEE, vol 86, issue 11, pages 2278-2324 (1998).
- [62] *Tensorflow*, <https://www.tensorflow.org/>.
- [63] V. Nair and G. E. Hinton, “Rectified Linear Units Improve Restricted Boltzmann Machines”, Proceedings of the 27th International Conference on International Conference on Machine Learning, ICML’10, U.S.A., 807–814, Omnipress (2010).

- [64] A. Y. Ng, “Feature selection, L1 vs. L2 regularization, and rotational invariance,” Proceedings of the International Conference on Machine Learning (2004).
- [65] S. Ioffe and C. Szegedy, “Batch Normalization: Accelerating Deep Network Training by Reducing Internal Covariate Shift”, ICML (2015) [arXiv:1502.03167v3 [cs.LG]].
- [66] N. Srivastava *et al.*, “Dropout: A Simple Way to Prevent Neural Networks from Overfitting”, Journal of Machine Learning Research **15** (2014) 1929-1958.
- [67] C. E. Nwankpa, W. Ijomah, A. Gachagan, and S. Marshall, “Activation Functions: Comparison of Trends in Practice and Research for Deep Learning ”, arXiv:1811.03378 (2018).
- [68] D. P. Kingma and J. Ba, “Adam: A Method for Stochastic Optimization”, 3rd International Conference for Learning Representations, San Diego (2015) [arXiv:1412.6980v9 [cs.LG]].
- [69] Y. Li, J. Yang, Y. Song, L. Cao, J. Luo, L. Li, “Learning from Noisy Labels with Distillation,” arXiv:1703.02391 (2017).
- [70] T. Fawcett, ”An introduction to ROC analysis”, Pattern Recognition Letters **27** 8 861 - 874 (2006)
- [71] F. Ratnikov [CMS Collaboration], Conf. Proc. C **100901**, 297 (2010) [arXiv:1111.1635 [hep-ex]].
- [72] S. Banerjee, G. Blanger, B. Bhattacharjee, F. Boudjema, R. M. Godbole and S. Mukherjee, “Novel signature for long-lived particles at the LHC,” Phys. Rev. D **98**, no. 11, 115026 (2018) doi:10.1103/PhysRevD.98.115026 [arXiv:1706.07407 [hep-ph]].